JOURNAL OF SYNCHROTRON RADIATION

ISSN 1600-5775

3D-printed photo-spectroelectrochemical devices for *in situ* and *in operando* X-ray absorption spectroscopy investigation

Elisabetta Achilli,[a] Alessandro Minguzzi,[b] Alberto Visibile,[b] Cristina Locatelli,[b] Alberto Vertova,[b,c,d] Alberto Naldoni,[e] Sandra Rondinini,[b,c,d] Ferdinando Auricchio,[f] Stefania Marconi,[f] Martina Fracchia[a] and Paolo Ghigna[a]*

[a]Dipartimento di Chimica, Università di Pavia, Via Taramelli 16, Pavia 27100, Italy, [b]Dipartimento di Chimica, Università degli Studi di Milano, Via Golgi 19, Milan 20133, Italy, [c]Istituto di Scienza e Tecnologia Molecolari, Consiglio Nazionale delle Ricerche, Via Golgi 29, Milan 20133, Italy, [d]Consorzio Interuniversitario Nazionale per la Scienza e Tecnologia dei Materiali – INSTM, Milano Unit, Via Golgi 19, Milan 20133, Italy, [e]CNR – Istituto di Scienze e Tecnologie Molecolari, Via Golgi 19, Milan 20133, Italy, and [f]Dipartimento di Ingegneria Civile e Architettura, Università di Pavia, Via Ferrata 3, Pavia 27100, Italy. *Correspondence e-mail: paolo.ghigna@unipv.it

Received 25 August 2015
Accepted 20 December 2015

Edited by R. W. Strange, University of Liverpool, UK

Keywords: 3D printing; *in situ* and *in operando* XAS; photo-electrochemistry; compact environmental cells; photoanodic reactions.

Three-dimensional printed multi-purpose electrochemical devices for X-ray absorption spectroscopy are presented in this paper. The aim of this work is to show how three-dimensional printing can be a strategy for the creation of electrochemical cells for *in situ* and *in operando* experiments by means of synchrotron radiation. As a case study, the description of two cells which have been employed in experiments on photoanodes for photoelectrochemical water splitting are presented. The main advantages of these electrochemical devices are associated with their compactness and with the precision of the three-dimensional printing systems which allows details to be obtained that would otherwise be difficult. Thanks to these systems it was possible to combine synchrotron-based methods with complementary techniques in order to study the mechanism of the photoelectrocatalytic process.

1. Introduction

Synchrotron radiation has nowadays grown into an essential tool for the study of the changes in terms of charge state, local geometric and electronic environment of target elements during the occurrence of particular physico-chemical phenomena, which are in turn triggered by variations in temperature, pressure or by electrochemical perturbations (Filez *et al.*, 2014; Tian *et al.*, 2014; Mansour *et al.*, 2002; Hillman *et al.*, 2011). One of the main limitations lies in the adaptation of the beamlines to the different experimental needs: in many cases it is difficult to create adequate setups to monitor and control the physicochemical conditions of the sample. In addition, there is an increasing need for detailed study of systems in their real working conditions: this is particularly true in the field of catalysis where *in situ* and *in operando* techniques are gaining increasing attention (Frenkel *et al.*, 2012). The purpose of this work is to show how three-dimensional (3D) printing can be an effective tool for the construction of multi-purpose cells for *in situ* and *in operando* experiments with synchrotron radiation. As a case study, here we describe two different types of cells (A and B, respectively) for X-ray absorption spectroscopy (XAS) experiments on photoanodes for photoelectrochemical water splitting. This is in turn a challenging topic since these devices represent in principle the ideal energy-conversion systems,

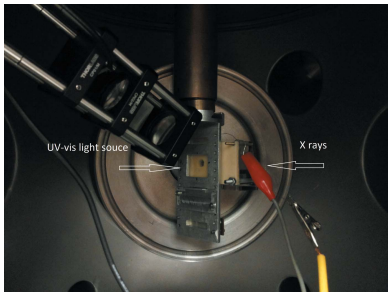

allowing the direct production of hydrogen from sunlight. The photoanodes we investigated are composed of an electrocatalytic domain (IrO_x), which is characterized by high activity as catalyst for the oxygen evolution reaction (OER) in the water-splitting process (Yamanaka, 1989; Steegstra & Ahlberg, 2012; Blakemore *et al.*, 2011), coupled to a semiconductor part (hematite, α-Fe_2O_3), which is sensitive to UV–Vis light. The investigation of photoelectrochemical water splitting represents a step of a more complete research plan, aimed at studying the mechanism and the kinetics of electrocatalytic reactions (Minguzzi *et al.*, 2013, 2014, 2015; Achilli *et al.*, 2014). The study of photoelectrochemical architectures (Fujishima & Honda, 1972) would shed light onto the role of the electrocatalyst when coupled to a semiconductor, providing a link between electrochemistry and photochemistry. It is important to note that the coupling between the semiconductor domain and the electrocatalytic moiety implies limits on the illumination by both X-rays and UV–Vis light.

Fig. 1 shows a scheme of the photoanode: it is composed of a bilayer architecture with the semiconductor part deposited onto a fluorine-doped tin oxide (FTO) substrate, which is transparent in the visible range but strongly absorbs in the near-UV. On the other hand, IrO_x strongly absorbs in the visible region. Then, in each experiment, UV–Vis illumination could occur on different sides of hematite according to the best opportuneness. The X-ray probe is then used for the investigation of local electronic changes in the IrO_x overlayer triggered by illumination of Fe_2O_3. The main limitation of the X-ray probe lies here in the attenuation coefficient of the other materials present. The presence of the hematite and FTO on the back-side of the electrocatalytic film prevents us from irradiating the system with X-rays from the back-side, and in addition forbids the use of transmission geometry. Consequently, XAS investigation should take place at the other side of the IrO_x film, which is in direct contact with the

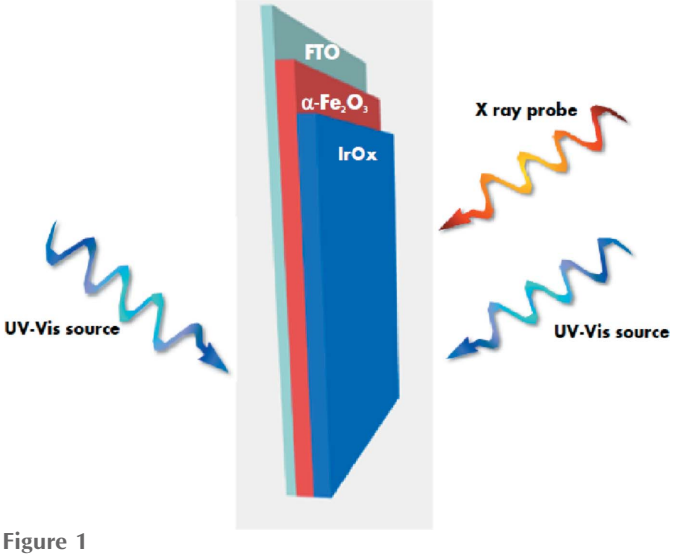

Figure 1
Photoanode architecture: the IrO_x film is in contact with the Fe_2O_3 deposited onto the FTO substrate.

electrolytic solution, and in fluorescence mode. With respect to the water attenuation coefficient at the Ir L_{III}-edge, the solution layer cannot be thicker than 1 mm. A photo-spectroelectrochemical cell for hosting such a photoanode should also allow a three-electrode assembly where the working electrode (at which the process of interest takes place) is combined with a counter electrode (a Pt foil) and a reference (usually Ag/AgCl). It is important to point out that in these small-sized electrochemical cells small channels and holes are present that are difficult to obtain manually or with conventional tools. These channels and holes should guarantee the electrical contact between the electrodes *via* the electrolyte. Another requirement for these devices is the resistance against X-rays in order to avoid the formation of holes in the material and the subsequent loss of content. The employment of a 3D printer based on the use of photopolymers represents the easiest and fastest way to produce efficient photo-spectroelectrochemical devices characterized by details that would be difficult to obtain using standard subtractive manufacturing technologies.

The first example of the use of 3D printing of a cell for spectroscopy dates back to a few years ago (Symes *et al.*, 2012), but, to our best knowledge, 3D printing has not yet been employed for building photoelectrochemical devices for *in situ* and *in operando* experiments with synchrotron radiation.

2. Design of the photo-spectroeletrochemical devices

The photo-spectroelectrochemical devices described in this work are entirely made of a photopolymer resin.

2.1. Cell type A

As shown in the scheme presented in Fig. 2(*a*), the device is composed of two parts. Side 1 in Fig. 2(*a*) is the cell main body, while side 2 is a rectangular cover. The two parts are assembled by means of screws and bolts, inserting an O-ring ensuring tightness against electrolyte leakage. The frontal circular window is used for illumination by both UV–Vis and X-rays. The internal cell volume is then filled with the elec-

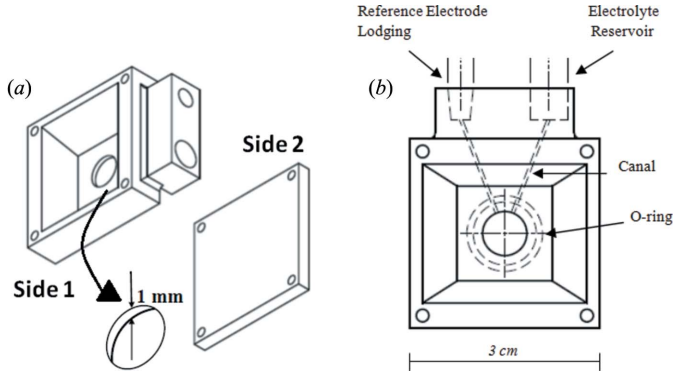

Figure 2
Design of cell type A: rectangular plate and cover with hole (*a*) and schematic representation of the canals connecting the reference and counter electrodes holders to the inner part of the cell (*b*).

trolyte as explained below. In this case, the thickness of the frame defined by the two arrows in Fig. 2(*a*) is limited to 1 mm, due to the absorption of water at the energy of the Ir L_{III}-edge (the absorbtion length for water at 11200 eV is 2.5 mm).

The rectangular shape is ideal for adding an upper external part that in turn allows a stable lodging of the reference electrode. The lodging constitutes a rectangular block with two cylindrical holes, of which one is used for housing the reference electrode and the other for filling the cell, once assembled, with the electrolyte by means of a syringe, and also works as an electrolyte reservoir. Both holes are connected to the inner part of the cell by means of small canals, whose diameter is 500 µm (Fig. 2*b*): this diameter is in turn dictated by the thickness of the 1 mm frame as detailed above. The counter electrode consists of a mylar square film, half of which is covered with a Pt/C+Nafion mixture. The latter is deposited by dropcasting over the mylar while kept on a laboratory hot plate. The electrical contact is ensured by Ag epoxy (EPO-TEK® H20E) and a Cu wire. The electrode is glued onto the frontal face of the cell using melted Parafilm®. The counter electrode thus also works as a closure of the whole internal cell volume.

The electrochemical device with and without the three-electrode assembly is shown in Fig. 3. The stable architecture achieved by means of this design allows the best conditions for performing photo-electrochemical measurements to be obtained. In this case the working electrode is the photoanode made of two parts, namely the electrocatalytic domain, IrO_x, which is subjected to the XAS investigation, and a semiconductor part Fe_2O_3, which is illuminated by an UV–Vis diode. The cell contains the electrolyte solution with a controlled thickness and presents a frontal window allowing illumination by X-ray photons.

This electrochemical cell was employed to investigate electrodeposited IrO_x overlayers. Hematite/IrO_x photoanodes were prepared as described by Marelli *et al.* (2014). In the present case, the deposition of IrO_x required 800 s.

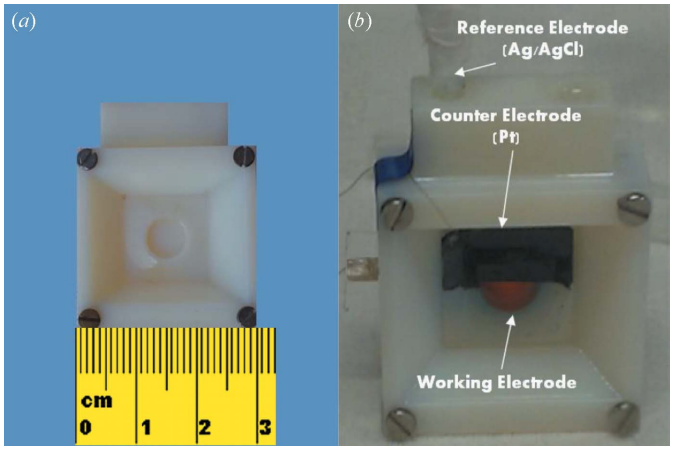

Figure 3
Image of the assembled photo-spectroelectrochemical cell of type A without (*a*) and with (*b*) the three-electrode setup.

2.2. Cell type B

The scheme of cell B, that is clearly a modification of cell A, is illustrated in Figs. 4(*a*) (front side) and 4(*b*) (back side). There are two main differences of this cell if compared with cell A. The first lies in the presence of an additional electrolite reservoir (Fig. 4*d*) in the main body of the device. This part is open at the upper side and is electrically connected to the photoanode by the elctrolyte. The design of this feature is aimed at: (i) obtaining room devoted to the lodging of the counter electrode in direct electrical contact with the photoanode; and (ii) having a larger static reservoir for the electrolyte to cope with possible radiation damage (local heating, radical formation, *etc.*) induced by the X-ray beam. The second important characteristic of this electrochemical cell is represented by the circular hole generated in the rectangular cover. This feature provides a window on the working electrode and is accomplished in order to perform UV–Vis illumination at the back-side of the hematite, thus avoiding absorption in the visible region by the IrO_x layer.

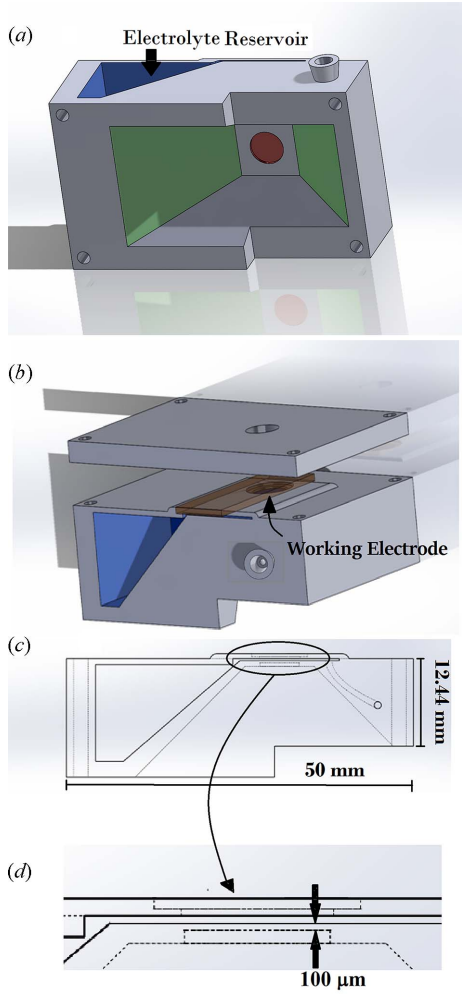

Figure 4
Scheme of the photo-spectroelectrochemical cell of type B showing the electrolyte reservoir (*a*), the rectangular cover with circular hole (*b*), the curved canal connecting the reference electrode to the inner part of the cell (*c*) and the working electrode lodging (*d*).

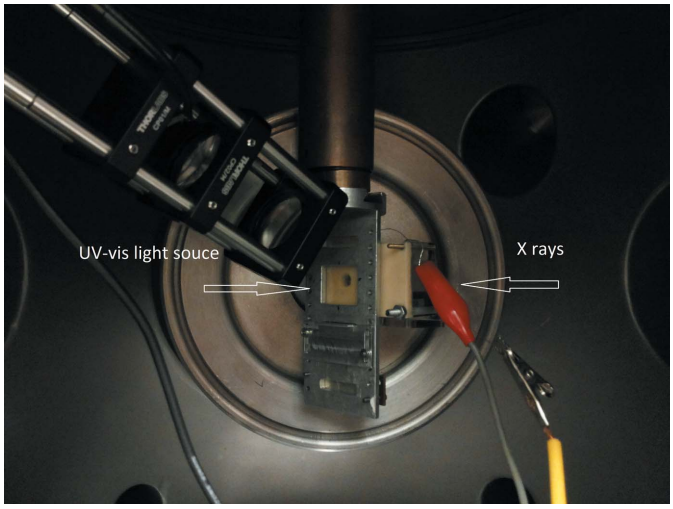

Figure 5
Photograph of the assembled photo-spectroelectrochemical cell of type B, mounted in the experimental hutch. UV–Vis illumination is carried out on the left-hand side by means of a solar simulator lamp whereas the X-ray illumination takes place on the other side of the cell.

The main body of the device and the rectangular cover are held together by means of screws and bolts, and an O-ring is inserted in order to ensure tightness against solution leakage. The rectangular-shaped electrolyte chamber presents an upper slot, ideal for the insertion of the Pt counter electrode. The lodging for the reference electrode is achieved by a hole generated in the upper part. This is connected to the electrolyte chamber by means of a curved canal with a diameter equal to 500 µm as one can see in the cross section illustrated in Fig. 4(*c*). In addition, this second cell has a 100 µm-thick window for X-ray illumination that is directly printed on the front side, ensuring a proper sealing against the back pressure of the electrolyte solution. The realisation of such details would not be possible (or very difficult to realise) with the traditional and manual instrumentation. Fig. 5 shows a photograph of the electrochemical device with the three-electrode assembly mounted in the experimental hutch of the LISA beamline (BM08) at ESRF, where all the experimental results described in this paper were obtained: UV–Vis illumination is carried out on the left-hand side by means of a solar simulator lamp whereas the X-ray illumination takes place on the other side of the cell.

Cell type B was used to study photoelectrodeposited IrO_x overlayers. In this case, the hematite photoanode was prepared according to the procedure reported by Malara *et al.* (2015). IrO_x is then photoelectrodeposited by a 0.45 m*M* $IrCl_3$ solution at pH = 13, after immersing FTO@α-Fe_2O_3 in the solution together with a saturated calomel electrode and platinum sheet as reference and counter electrodes, respectively. The deposition lasted 15 min and was carried out at +0.6 V relative to the saturated calomel electrode (SCE) while the photoelectrode was kept under illumination using a LED (λ = 400 nm, LED ENGINE LZ1-00UA00) as a light source.

3. Cell fabrication

The photo-spectroelectrochemical devices are manufactured using a photopolymer-based printer (Objet 30 Pro, Objet-Stratasys). This technology was selected among different 3D printing solutions available on the market because of its ability to print very small parts with high resolution and using a material that is resistant to chemicals. The printer uses photopolymeric resins that are laid down on the printing bed in a liquid form and polymerized using a UV lamp. The device is printed at a layer resolution of 28 µm, that is the height of each deployed layer, while the in-plane printing error is about 1 µm per 1 mm. This is well appropriate to the diameter of the channels for the reference electrode and for the electrolyte reservoir (500 µm, as mentioned above).

The printer can deploy one material at a time, in combination with a support material that can be removed using a water jet machine and a sodium hydroxide solution. The presence of the support material in all the inner cavities was taken into account during the device design. Actually, all the inner channels have been designed with the minimum level of curved parts, in order to facilitate the cleaning process.

The devices are printed using the VeroWhite material, an opaque rigid photopolymeric polyacrilic resin characterized by an adequate stiffness and resistance to chemicals.[1]

An adequate resistance to temperatures and mechanical stresses forced by the experimental conditions characterizes this material. Actually, the resin has a softening temperature of 52–54°C (measured with ASTM standard DMA) and has a heat deflection temperature of about 45–50°C (measured with ASTM standard D-648-06 and D-648-07). Since the experimental procedure is carried out in contact with a liquid, water absorption represents another important feature for consideration; actually, the prototyped object always has a little porosity because of the layering process that builds it. The water absorption parameter ranges from 1.1% to 1.5% within 24 h. Since each experimental test lasts for less than 8 h, the devices can be considered as waterproof for this application.

The printer is able to realise an entire set in about 2 h. After printing, the device components are cleaned first using a water jet machine, paying attention to not damaging the thin walls. After that, the parts are immersed in a solution of water (90%) and sodium hydroxide (10%) to facilitate the removal of the support material. A thin wire has been used to ensure a good cleaning of the inner channels.

4. XAS results

The capabilities of the photo-spectroelectrochemical cells described are illustrated in this section.

Before discussing the X-ray absorption results, it is important to show that the 3D-printed electrochemical devices actually work. A comparison between a cyclic voltammetry obtained by means of a 3D-printed XAS cell and one obtained

[1] http://usglobalimages.stratasys.com/Main/Secure/MSDS/Rigid%20Opaque%20Materials/DOC-06124--Objet-VeroWhitePlus-RGD835-US.pdf?v=635508837056815513.

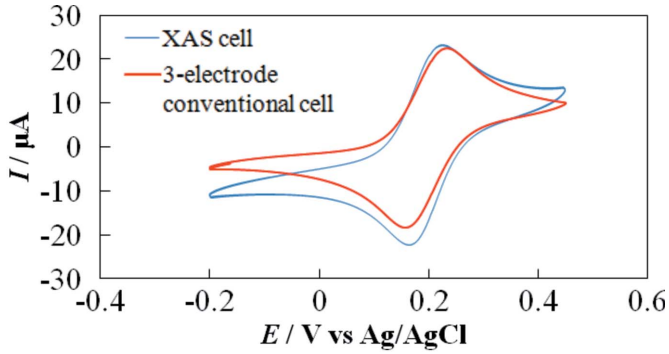

Figure 6
Comparison between a cyclic voltammetry obtained by means of a 3D printed XAS cell (blue line) and one obtained by means of a standard electrochemical cell (red line). These were performed between −0.2 and 0.4 V *versus* Ag/AgCl (KCl 1 *M*) at 20 mV s^{-1} in ferrocene methanol 1 m*M* in $KClO_4$ 0.1 *M*. Working electrode: Pt foil.

by means of a standard electrochemical cell is illustrated in Fig. 6. These electrochemical measurements were performed between −0.2 and 0.4 V *versus* Ag/AgCl (KCl 1 *M*) at 20 mV s^{-1} in ferrocene methanol 1 m*M* in $KClO_4$ 0.1 *M*. The working electrode was a Pt foil. The signals clearly show that the cell response is very similar in the two cases, thus probing the conformity between the electrochemical behaviours.

Fig. 7 illustrates XAS results obtained *in situ* and *in operando* by means of the 3D-printed electrochemical devices previously described. Two different types of sample have been considered: electrodes onto which the IrO_x film was electrodeposited (Figs. 7*a*–7*c*) and electrodes onto which the IrO_x film was photodeposited (Fig. 7*d*).

Fig. 7(*a*) shows Ir L_{III} XANES spectra obtained at two different potential values: 0.4 and 1.4 V relative to the reversible hydrogen electrode (RHE) (in the latter case oxygen evolution takes place) by means of the A type cell. The spectra of $IrCl_3$ and IrO_2 standard materials are added as better references for Ir(III) and Ir(IV), respectively. Transitions from the Ir 2*p* levels to continuum states and to 5*d* localized states give rise to steps and peaks (white lines). The energy position of the peak maximum is directly associated with the Ir oxidation state: a shift to a larger potential value corresponds to an oxidation process.

When the applied potential is 0.4 V the peak maximum is situated between that of $IrCl_3$ and IrO_2, thus indicating that the mean oxidation state is between (III) and (IV). Under oxygen evolution conditions, when the potential is equal to 1.4 V, the peak maximum is shifted towards larger energy values. This suggests that the oxidation state of the photoabsorber is very close to Ir(IV). This corresponds, considering the ohmic drops in the α-Fe_2O_3 layer, to what has been previously described by some of us (Minguzzi *et al.*, 2014, 2015) by using a much larger volume cell.

In Figs. 7(*b*) and 7(*c*) the response of the IrO_x layer to the illumination of α-Fe_2O_3 by UV–Vis light is shown for two different applied potentials: 0.4 V (Fig. 7*b*) and 0.8 V (Fig. 7*c*). The normalized XANES spectra acquired in UV–Vis light (red line) and dark conditions (blue line) are illustrated. Their

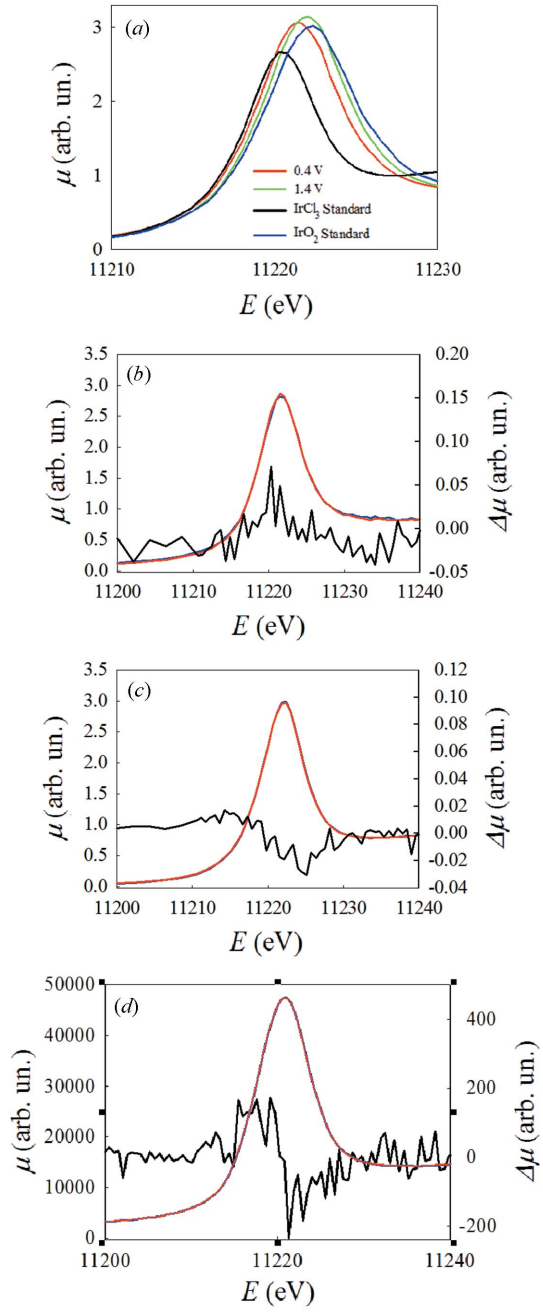

Figure 7
XAS results obtained *in situ* and *in operando* by means of the 3D-printed electrochemical devices. Two different types of sample have been considered: electrodes onto which the IrO_x film was electrodeposited (*a*, *b*, *c*) and electrodes onto which the IrO_x film was photoelectrodeposited (*d*). (*a*) Ir L_{III} XANES spectra acquired *in situ* at two different potential values: 0.4 V (red line) and 1.4 V (green line) *versus* RHE. The spectra of $IrCl_3$ (black line) and IrO_2 (blue line) standard materials are plotted as references for Ir(III) and Ir(IV), respectively. (*b*, *c*) Ir L_{III} normalized XANES spectra acquired at a constant potential value equal to 0.4 V (*b*) and to 0.8 V (*c*) under UV–Vis light conditions (red line) and dark conditions (blue line), and the respective differences (black lines) obtained from the subtraction of the spectrum under dark conditions from that acquired under UV–Vis light conditions. (*d*) Response of the photoanode to the illumination by UV–Vis light when the IrO_x layer is prepared by photo-electrodeposition, recorded at a potential of 1.56 V relative to RHE. The signal is different between the XANES spectrum recorded in the presence and that recorded in the absence of the UV–Vis illumination (light − dark).

differences (represented by the black lines), resulting from the subtraction of the spectrum acquired in light conditions from that observed in dark conditions, are different in the two cases but very small. However, taking into account that the signal is recorded *in situ* by means of a photo-spectroelectrochemical device, these differences can be considered as significant. For an applied potential equal to 0.4 V the difference is positive; for an applied potential equal to 0.8 V the difference is negative.

As a further example, Fig. 7(*d*) shows the response of the photoanode to the illumination by UV–Vis light when the electrodic layer is prepared *via* photo-electrochemical deposition. In this case, measurements were performed by means of the electrochemical cell of type B. The red line and the blue line are the XANES spectra acquired in the presence and absence of UV–Vis light illumination, respectively. The difference between them is indicated by the black line. Its trend clearly accounts for a peak shift towards lower energy values under UV–Vis illumination.

A detailed explanation of the mechanism and the kinetics of the photo-electrochemical processes involved in the results reported above is well beyond the aim of this paper and it will be the object of future work. These results, however, show that the experimental setup provides a key tool for monitoring the UV–Vis light driven variations in the hole density of iridium *5d* states under different applied potentials. What can be noted here is that the IrO_x overlayers prepared by different methods (by electrochemical or photoelectrochemical deposition) respond differently to UV–Vis illumination.

5. Conclusions

In the current research work we designed and built multi-purpose photo-spectroelectrochemical devices for *in situ* and *in operando* X-ray absorption spectroscopy by means of a 3D printer. Thanks to these systems it was possible to combine synchrotron-based methods with complementary techniques. In particular we created two types of photo-spectro-electrochemical cell for investigating photoelectrochemical water splitting providing a key link between spectroscopy and electrochemistry and photochemistry.

The main characteristics of these electrochemical devices are summarized below:

(i) The devices are compact and small enough to allow an easy and fast experimental setup in the beamline hutch.

(ii) Thanks to the precision of the 3D printing system, it is possible to achieve detail that otherwise would be difficult to obtain. For example, it is possible to control the thickness of the electrolytic solution avoiding problems associated with X-ray attenuation coefficient by water. Furthermore, we can obtain small and curved canals for the counter and reference electrodes ensuring electric contact between the different parts of the cell.

(iii) The cell geometry is easily adaptable for other experiments, for example for studying different materials or for performing RIXS or XRD. In particular, the experiments described here were performed at the Ir L_{III}-edge (11215 eV). However, the design of cell B allows softer X-rays to be used thanks to the fact that the X-ray window is printed and can in principle be made thinner to cope with the smaller penetration depth at low energies, still ensuring a proper stiffness for sustaining the back pressure of the electrolyte.

Experiments carried out by means of these photo-spectro-electrochemical devices allowed measurements at different potential values to be performed, including those where oxygen evolution is expected to occur. Furthermore, thanks to specific details mentioned above, it was possible to study the different responses of the catalyst under UV–Vis light and dark conditions. Results obtained led to a better understanding of the mechanism and the kinetics associated with the photoelectrocatalytic process of water splitting.

As a final remark, we note that the small volume parts of the photo-spectroelectrochemical devices described here could hardly be fabricated without the 3D printing technology. It is quite straightforward to expect that this technology will be of increasing importance in the creation of environmental chambers for *in situ* and *in operando* synchrotron radiation experiments.

Acknowledgements

BM08-LISA at ESRF is kindly acknowledged for provision of beam time. The beamline staff, and in particular Dr Francesco d'Acapito, are also kindly acknowledged for valuable help during the experiment setup and data collection.

References

Achilli, E., Minguzzi, A., Lugaresi, O., Locatelli, C., Rondinini, S., Spinolo, G. & Ghigna, P. (2014). *J. Spectrosc.* **2014**, 480102.
Blakemore, J. D., Schley, N. D., Olack, G. W., Incarvito, Ch. D., Brudvig, G. W. & Crabtree, R. H. (2011). *Chem. Sci.* **2**, 94–98.
Filez, M., Poelman, H., Ramachandran, R. K., Dendooven, J., Devloo-Casier, K., Fonda, E., Detavernier, C. & Marin, G. B. (2014). *Catal. Today*, **229**, 2–13.
Frenkel, A. I., Rodriguez, J. A. & Chen, J. G. (2012). *ACS Catal.* **2**, 2269–2280.
Fujishima, A. & Honda, K. (1972). *Nature (London)*, **238**, 37–38.
Hillman, R., Skopek, M. A. & Gurman, J. (2011). *Phys. Chem. Chem. Phys.* **13**, 5252–5263.
Malara, F., Minguzzi, A., Marelli, M., Morandi, S., Psaro, R., Dal Santo, V. & Naldoni, A. (2015). *ACS Catal.* **5**, 5292–5300.
Mansour, A. N., Smith, P. H., Baker, W. M., Balasubramanian, M. & McBreen, J. (2002). *Electrochim. Acta*, **47**, 3151–3161.
Marelli, M., Naldoni, A., Minguzzi, A., Allieta, M., Virgili, T., Scavia, G., Recchia, S., Psaro, R. & Dal Santo, V. (2014). *Appl. Mater. Interfaces*, **6**, 11997–12004.
Minguzzi, A., Locatelli, C., Lugaresi, O., Achilli, E., Cappelletti, G., Scavini, M., Coduri, M., Masala, P., Sacchi, B., Vertova, A., Ghigna, P. & Rondinini, S. (2015). *ACS Catal.* **5**, 5104–5115.
Minguzzi, A., Lugaresi, O., Achilli, E., Locatelli, C., Vertova, A., Ghigna, P. & Rondinini, S. (2014). *Chem. Sci.* **5**, 3591–3597.
Minguzzi, A., Lugaresi, O., Locatelli, C., Rondinini, S., D'Acapito, F., Achilli, E. & Ghigna, P. (2013). *Anal. Chem.* **85**, 7009–7013.

Steegstra, P. & Ahlberg, E. (2012). *Electrochim. Acta*, **68**, 206–213.
Symes, M. D., Kitson, P. J., Yan, J., Richmond, C. J., Cooper, G. J. T., Bowman, R. W., Vilbrandt, T. & Cronin, L. (2012). *Nat. Chem.* **4**, 349–354.
Tian, Y., Etschmann, B., Mei, Y., Grundler, P. V., Testemale, D., Hazemann, J., Elliott, P., Ngothai, Y. & Brugger, J. (2014). *Geochim. Cosmochim. Acta*, **129**, 77–95.
Yamanaka, K. (1989). *Jpn. J. Appl. Phys.* **28**, 632–637.